Steady saturation distribution in hydrophobic gas-diffusion layers of polymer electrolyte membrane fuel cells: A pore-network study

Kyu-Jin Lee[a], Jin Hyun Nam[b,*], Charn-Jung Kim[a]

[a] School of Mechanical and Aerospace Engineering, Seoul National University, Seoul 151-742, Republic of Korea
[b] School of Mechanical and Automotive Engineering, Kookmin University, 861-1 Jeongneung-dong, Seongbuk-gu, Seoul 136-702, Republic of Korea

ARTICLE INFO

ABSTRACT

A pore-network model is developed to simulate liquid water transport in a hydrophobic gas-diffusion layer (GDL) during the operation of polymer electrolyte membrane fuel cells (PEMFCs). The steady saturation distribution in GDLs is determined through a numerical procedure using a pore-network model combined with invasion-percolation path-finding and subsequent viscous two-phase flow calculation. The simulation results indicate that liquid water transport in hydrophobic GDLs is a strongly capillary-driven process that almost reaches the pure invasion-percolation limit with zero capillary number. A uniform flux condition is found to better reflect the actual phenomenon occurring at the inlet boundary for liquid water entering a GDL than a uniform pressure condition. The simulation further clarifies the effect of the invaded pore fraction at a uniform-flux inlet boundary in modifying water transport in GDLs. Finally, the effect of the GDL thickness on the steady saturation distribution is investigated.

© 2009 Elsevier B.V. All rights reserved.

1. Introduction

A polymer electrolyte membrane fuel cell (PEMFC) is an efficient and clean energy-conversion device that generates electrical power through the direct electrochemical combination of fuel and an oxidant [1,2]. Polymer electrolyte membrane fuel cells are operated at relatively low temperatures of around 80 °C, which enables good transient characteristics, that include short start-up times and a fast response to load change. Thus, PEMFCs are considered to be the most suitable fuel cell technologies for automotive power generation, an application that requires a high power density and good dynamic behaviour. Lately, water and heat management has attracted much research as a way to enhance the system-level performance of PEMFCs [3,4].

Flooding in hydrophobic gas-diffusion layers (GDLs) is one of the most important water-management issues that is closely connected to the performance of PEMFCs when operating at high current densities. Accordingly, many numerical studies have been conducted to understand water transport behaviour and to predict the saturation distribution in the GDLs of PEMFCs [5–14]. It should be noted that these numerical models were based on continuum transport theories for two-phase flow in porous media. Extensive experimental research has also been performed to visualize liquid water trans-

port or to quantitize the liquid water content in GDLs by means of microscopic observation [15,16], magnetic resonance imaging (MRI), X-ray tomography [17,18], and neutron radiography [19,20].

High-resolution neutron radiography studies have been reported very recently [21–23], wherein the liquid water content in GDLs was resolved at scales of several micrometers. The saturation distribution obtained from the resulting images [21–23] suggested that more complex processes, in addition to continuum two-phase flow, might operate during the water transport in GDLs. Fundamental modelling studies have also recently been conducted to gain a better knowledge of water transport in GDLs based on the full-morphological approach [24], the Lattice–Boltzmann method [25], and the pore-network model [26–30].

Recent pore-network studies have shown that water transport in a hydrophobic GDL is a strongly capillary-driven process [28–30]. In fact, this result is consistent with the phase diagram for two-phase drainage flow proposed by Lenormand et al. [31]. According to the work reported in [31,32], invasion-percolation with capillary fingering is expected to be a main transport mechanism for two-phase liquid water transport in GDLs during the operation of PEMFCs. Invasion-percolation water transport results in a concave saturation distribution along the flow direction [32], which is different from the convex saturation distribution predicted by conventional continuum two-phase flow models.

In this investigation, a simplified pore-network model is developed to simulate efficiently steady water transport in hydrophobic GDLs by combining invasion-percolation path-finding and subse-

quent viscous two-phase flow calculation. The long calculation time required for full transient pore-network simulations could be avoided in the simplified pore-network model, which facilitates evaluation of the effects of various parameters in shorter times. Utilizing the model, this study first investigates the validity of two inlet boundary conditions for liquid water entering the GDLs as discussed by Lee et al. [30], i.e., a uniform pressure condition and a uniform flux condition. Then, the effect of liquid water flux is studied to examine the dominance of capillary forces over viscous forces during water transport in hydrophobic GDLs. The water management role of microporous layers (MPLs), recently proposed by Nam et al. [33] and Gostick et al. [34], is also validated by varying the invaded pore fraction at a uniform-flux inlet boundary for liquid water entering the GDLs. Finally, the effect of the GDL thickness on the steady liquid water saturation distribution is investigated.

2. Theory and calculation

2.1. Liquid water transport in GDLs

Transient liquid water transport in a hydrophobic GDL during the operation of a PEMFC is a two-phase drainage process where an invading non-wetting fluid (liquid water) displaces a defending wetting fluid (air) that initially filled the porous GDL. This process is characterized by a small capillary number ($Ca \equiv \mu_{inv} q / \sigma \cos \theta$) of about 10^{-7}–10^{-8} and a moderate viscosity ratio ($M \equiv \mu_{inv}/\mu_{dis}$) of around 10 [28–30]. Such a small capillary number is due largely to the small volume flux of liquid water, q_{inj}, injected into a GDL that, in turn, is proportional to the water generation rate in a catalyst layer (CL). For example, a current density of 1 A cm^{-2} roughly corresponds to a q_{inj} of about 10^{-6} m s^{-1}.

The small value of Ca encountered during the operation of a PEMFC suggests that capillary forces rather than viscous forces dominate liquid water transport in a GDL. According to the phase diagram for the drainage processes [31], liquid water transport in a hydrophobic GDL corresponds to the capillary fingering regime, wherein this regime is characterized by the formation of long and meandering transport paths due to preferential invasion of non-wetting fluids into the pores of lower capillary entry pressures [31,32]. Previous pore-network studies [28–30] have also demonstrated that liquid water transport in a GDL is a strongly capillarity-driven process that is dominated by the invasion-percolation process with capillary fingering.

2.1.1. Capillary process

Liquid water spontaneously wets hydrophilic capillaries upon contact due to the adhesive force between the solid surface and liquid water. The contact angle, θ_w, that liquid water makes with air near the solid surface is less than 90° for hydrophilic capillaries. By contrast, liquid water does not spontaneously wet hydrophobic capillaries, and the contact angle becomes $\theta_w > 90°$. Thus, the liquid water pressure, p_w, is higher than the ambient air pressure, p_a, in hydrophobic capillaries. This also implies that an additional pressure should be applied to make the liquid water penetrate hydrophobic capillaries.

The pressure drop across the water|air interface in circular capillaries, or the capillary pressure, p_c, is determined by the Laplace–Young equation [35]. In this study, the capillary pressure in hydrophobic GDLs is redefined for simplicity of calculation and presentation as:

$$p_c = p_w - p_a = \sigma |\cos \theta_w| \left(\frac{1}{R_1} + \frac{1}{R_2} \right) = \frac{2\sigma |\cos \theta_w|}{r_{w/a}} \quad (1)$$

where σ denotes the surface tension of water; R_1 and R_2 denote two principal radii of curvature; $r_{w/a}$ denotes the mean radius of curva-ture of the water|air interface defined as $r_{w/a} = 2(R_1^{-1} + R_2^{-1})^{-1}$. In Eq. (1), the capillary pressure in hydrophobic GDLs is treated as positive and equal to the gauge pressure of liquid water over the ambient air pressure. It should also be noted that the air pressure is generally uniform in GDLs during the steady operation of PEMFCs.

2.1.2. Condition of liquid water entering GDLs

The condition of liquid water at the interface between a GDL and a CL (or at the interface between a GDL and a MPL) is recognized as an important factor for water transport and saturation distribution in GDLs [33,34]. The following two conditions were previously considered for pore-network studies of liquid water transport in GDLs: a uniform pressure condition [28,29] and a uniform flux condition [30]. The former condition assumes that the liquid water pressure is spatially uniform at the inlet boundary of a GDL, as if a continuous liquid water reservoir is connected to all inlet pores. As a result, the liquid water flux becomes spatially non-uniform at the inlet boundary of the GDL. The uniform pressure condition can be implemented in pore-network models by connecting all the inlet pores to a virtual source pore that simulates the reservoir.

On the other hand, the uniform flux condition assumes that the liquid water flux is spatially uniform at the inlet boundary of a GDL, as if the liquid water is injected directly into each inlet pore. Thus, the liquid water pressure becomes spatially non-uniform at the inlet boundary of the GDL. This boundary condition can be implemented in pore-network models by prescribing a liquid water injection rate for randomly selected inlet pores. Lee et al. [30] discussed the validity of the two boundary conditions and suggested that a uniform flux condition is more consistent with the uniform generation of liquid water in a CL and subsequent invasion into a GDL. It was also shown that the uniform flux condition resulted in a longer transient period toward a higher steady saturation level in GDLs compared with the uniform pressure condition.

2.2. Pore-network model

Liquid water transport in hydrophobic GDLs is different from that in a bundle of straight hydrophobic capillaries. More complicated processes are expected to occur in real GDLs because of their complex pore structure, including irregular pore shapes and multiple pore connectivities. Nevertheless the fundamental mechanism of capillary transport in GDLs is believed to be similar to that explained with a bundle of straight hydrophobic capillaries.

The pore-network model is a proven numerical method that has been used to investigate various transport phenomena in porous media [36–40]. In the pore-network model, the complex pore structure in porous media is represented as a collection of cross-connected pores and throats. Although simplified, important characteristics of the pore structure can be preserved in the pore-network model by a discrete choice of pore-network geometries. Thus, pore-network models have also been used in theoretical research for liquid water transport in GDLs, either to determine the capillary pressure or relative permeability as a function of saturation [26,27], or to predict the saturation distribution [28–30].

2.2.1. Pore-network generation

The pore-networks for GDLs were constructed to be composed of cross-connected box-shaped pores and throats based on the prescribed geometrical parameters summarized in Table 1. First, cubic cells with a dimension of d_{cell} (=25 μm) were regularly arranged to fill the calculation domain ($n_x \times n_y \times n_z$ in cell number, or $L_x \times L_y \times L_z$ in physical length) as shown in Fig. 1(a). Box-shaped pores were then generated to have random dimensions of d_{px}, d_{py}, and d_{pz}, and positioned at the center of each cubic cell, as illustrated in Fig. 1(b). Each pore was connected to its neighboring

Table 1
Parameters for present pore-network model.

Parameter	Explanation	Value
$N_x \times N_y \times N_z$	Cell number of pore-network	$20 \times 20 \times 10$
$L_x \times L_y \times L_z$	Size of pore-network	$500\,\mu m \times 500\,\mu m \times 250\,\mu m$
L_{cell}	Unit cell size	$25\,\mu m$
l_{px}, l_{py}, l_{pz}	Dimension of pore body	17.5–$22.5\,\mu m$
l_{ta}, l_{tb}	Dimension of throat	5–$17.5\,\mu m$
$\bar{V}_p$	Mean pore volume[a]	$9899\,\mu m^3$ (SD $783\,\mu m^3$)
$\bar{r}_t$	Mean throat radius[a]	$5.33\,\mu m$ (SD $1.35\,\mu m$)
ε	Mean porosity	0.633 (SD 0.001)
K	Mean permeability	$3.39 \times 10^{-12}\,m^2$ (SD $7.9 \times 10^{-12}\,m^2$)
σ	Surface tension of water	$0.0645\,N\,m^{-1}$ at $70\,°C$
ρ_w	Density of water	$978\,kg\,m^{-3}$ at $70\,°C$
μ	Viscosity of water	$40.38 \times 10^{-5}\,Pa\,s$ at $70\,°C$
θ_w	Contact angle of water	$120°$
q_{inj}	Injection flux of water	$2\,A\,cm^{-2}$ equivalent

[a] Number-mean values (not volume-mean).

six pores through other box-shaped throats having random cross-sectional dimensions of d_{ta} and d_{tb}. The throats were also aligned to the center of each cubic cell face. The ranges for the pore dimensions were $0.7d_{cell} < d_{pi=xyz} < 0.9d_{cell}$ ($17.5\,\mu m < d_{pi=xyz} < 22.5\,\mu m$), and those for the throat dimensions were $0.2d_{cell} < d_{ti=ab} < 0.7d_{cell}$ ($5\,\mu m < d_{ti=ab} < 17.5\,\mu m$). Similar pore-network geometries have also been used in other studies [26,38].

The boundary conditions required for the pore-network calculation are explained in Fig. 1(a). An inlet and outlet boundary is located at the bottom and top plane of a pore-network, respectively. Liquid water is assumed to be introduced into a pore-network
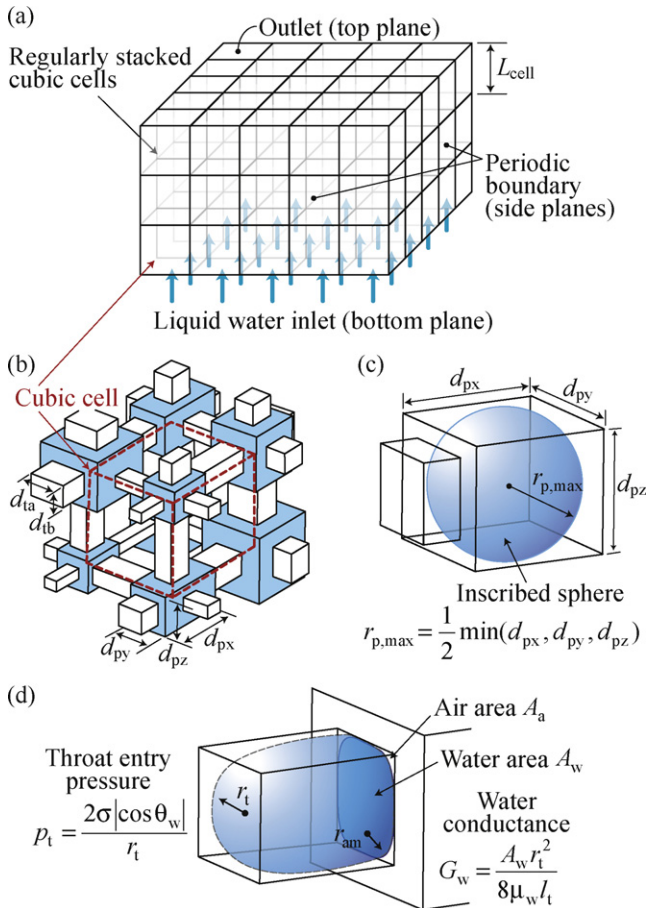

Fig. 1. Pore-network generation: (a) regularly arranged cubic cells, (b) box-shaped pores and throats, (c) liquid water droplet in box-shaped pore, and (d) invading front of liquid water through hydrophobic rectangular throat.

through the inlet boundary according to either a uniform pressure or uniform flux condition. The injected volume flux of liquid water, q_{inj}, at the inlet boundary is prescribed to be equivalent to a current density of $2\,A\,cm^{-2}$. A cyclic pore connectivity is assumed for the side planes of the calculation domain, as shown in Fig. 1(a), which infinitely extends the calculation domain in the x- and y-directions. The domain size of the pore-networks is chosen to be $20 \times 20 \times 10$ after a grid dependence test, which corresponds to the physical dimension of $500\,\mu m \times 500\,\mu m \times 250\,\mu m$ in the x-, y-, and z-directions.

It should be noted that the pore-network geometries constructed by the aforementioned generation rules are isotropic in nature. An anisotropic pore-network can be obtained by differently prescribing the unit cell size, the pore dimension and the throat dimension for both in-plane (x- and y-direction) and through-plane (z-direction) directions.

2.2.2. Pore-network parameters

Several geometrical parameters required for subsequent calculation steps were evaluated just after the pore-network generation. The pore volume, V_p, of a box-shaped pore was calculated as:

$$V_p = d_{px} \times d_{py} \times d_{pz}, \tag{2}$$

and the radius of the largest inscribed sphere, $r_{p,max}$, was determined as:

$$r_{p,max} = \frac{1}{2}\min(d_{px}, d_{py}, d_{pz}). \tag{3}$$

In Fig. 1(c), the inscribed sphere radius, $r_{p,max}$, corresponds to the largest mean radius of curvature of the water|air interfaces, $r_{w/a}$, attainable in box-shaped pores. Thus, the capillary pressure inside box-shaped pores has the lowest value at the saturation level corresponding to the situation shown in Fig. 1(c). The transition saturation, S_{tr}, is thus defined as:

$$S_{tr} = \frac{4\pi}{3}\frac{r_{p,min}^3}{V_p}, \tag{4}$$

which is the critical saturation for the minimum capillary pressure for a pore.

For throats, the cross-sectional area, A_t, was calculated as:

$$A_t = d_{ta} \times d_{tb}, \tag{5}$$

and the volume of a throat, $V_{t,ij}$, connecting pores i and j was determined as

$$V_{t,ij} = A_{t,ij} \times l_{t,ij}, \tag{6}$$

where $A_{t,ij}$ and $l_{t,ij}$ are the cross-sectional area and the length of the throat, respectively. From the pore-network generation rules, the length of a throat, $l_{t,ij}$, was calculated as:

$$l_{t,ij} = L_{cell} - \frac{1}{2}(d_{pi} - d_{pj}), \tag{7}$$

where d_{pi} or d_{pj} denotes a dimension of pores in the corresponding x-, y-, or z-direction.

The hydraulic radius is a parameter that influences both capillary and viscous transport through rectangular throats. The hydraulic radius of a throat, r_t, is determined as:

$$r_t = \frac{2A_t}{P_t} = \frac{d_{ta}d_{tb}}{d_{ta} + d_{tb}}, \tag{8}$$

where P_t denotes the perimeter of the throat, $2(d_{ta} + d_{tb})$. This hydraulic radius is expected to be similar to the mean radius of curvature, $r_{w/a}$, formed by liquid water invading a rectangular throat, as shown in Fig. 1(d).

The interface at the invading non-wetting phase front is called the main terminal meniscus (MTM) [36]. As shown in Fig. 1(d), there

is another type of water|air interface that is formed at the corners of a long non-circular throat. This interface is called the arc meniscus (AM). Since one principal radius of curvature becomes infinite as $R_1 \to \infty$, the radius of the arc meniscus, r_{am} (the same as the remaining principal radius, R_2), is equal to half the mean radius of curvature as $r_{am} = r_{w/a}/2$.

2.3. Pore-network calculation

The present pore-network model calculates the capillary pressure in pores as a main variable, while the capillary entry pressure and viscous resistance in throats are treated as varying transport parameters. The first step is to determine the percolated clusters of invaded pores and throats that constitute essential paths for the liquid water exhaust through a pore-network. Then, the steady two-phase flow through the percolated clusters is solved in order to determine the capillary pressure distribution required for a given liquid water flux. Finally, the spatial saturation distribution in the pore-network is calculated by summing the liquid volume in invaded pores and throats.

2.3.1. Invasion-percolation path-finding

The path-finding procedure was implemented by referring to the pure invasion-percolation transport of liquid water in hydrophobic porous media. According to the invasion-percolation rule, liquid water preferentially invades the throat with the smallest capillary entry pressure, p_t, defined as:

$$p_t = \frac{2\sigma|\cos\theta_w|}{r_t}. \tag{9}$$

Note that the hydraulic radius, r_t, is used to evaluate the mean radius of curvature for the water|air interface of invading fronts in rectangular throats.

If certain pores and throats in a pore-network are marked as 'invaded' at an instance during the invasion-percolation path-finding procedure, then a list can be made of throats that are connected to the invaded pores but not yet invaded. This list is called the 'throat searching pool,' which registers all possible throat passages available for the next advance or displacement of liquid water. Thus, a search for a minimum entry pressure should be performed for the throats in the throat searching pool.

Once a minimum capillary entry pressure is determined, it is used to update the capillary pressure of currently invaded pores. This pressure update is performed only for the invaded pores whose previously assigned capillary pressure is smaller than the determined minimum pressure. Then, a throat corresponding to the minimum entry pressure and its connected pore are marked as invaded for the next iteration. The above path-finding procedure is repeated until a throat that leads to the outlet boundary (the top plane of the domain) is finally invaded. As a final step, dead-end pores, which are connected to only one upstream pore, are searched in order to check that the capillary pressures of the dead-end pores are equal to those of their upstream pores.

For the uniform pressure condition, no pore was marked as invaded at the beginning of the invasion-percolation path-finding procedure. All throats that were connected to the inlet boundary (the bottom plane of the domain) were initially included in the throat searching pool and were maintained in the pool until they were invaded by having a minimum entry pressure during the procedure.

For the uniform flux condition, a slightly different approach was employed. A separate path-finding procedure was conducted for each of the randomly selected inlet pores by marking a selected pore as invaded (the throat between the pore and the inlet boundary was initially also marked as invaded). Then, the invaded pores and throats identified by the separate path-finding procedures were summarized to obtain the percolated clusters required for the uniform flux condition.

Note that the path-finding procedure determines both the essential clusters of invaded pores and throats due to invasion-percolation transport, as well as the corresponding capillary pressure distribution in those percolated pores.

2.3.2. Steady two-phase flow calculation

The steady liquid water transport was calculated only for the percolated clusters of invaded pores and throats determined by the preceding path-finding procedure. The viscous effects during the two-phase flow in hydrophobic GDLs were fully considered by including the viscous flow resistance of the throats. It should be noted that the air pressure, p_a, was not calculated, but assumed to be constant in this study. This approach may be justified from the following arguments. Random stacking of fibres in GDLs generally results in many small interstitial spaces that are difficult to be considered in pore-network models. These spaces in hydrophobic GDLs are too small for liquid water to penetrate, and thus, are generally available for air flow. In addition, the flow rate of oxygen during the steady operation of PEMFCs is very small, leading to negligible differences in the air pressure.

The conservation of volume at the steady-state is expressed as:

$$\sum_{j=\text{neiboring six pores}} Q_{i \to j} = 0, \tag{10}$$

where $Q_{i \to j}$ is the steady flow rate ($m^3\,s^{-1}$) from a pore i to its neighboring pore j. The constitutive equation for the steady flow rate, $Q_{i \to j}$, is written as:

$$Q_{i \to j} = G_{ij}[\max(p_{c,i}, p_{t,ij}) - \max(p_{c,j}, p_{t,ij})], \tag{11}$$

where $p_{c,i}$ and $p_{c,j}$ are the capillary pressures in the pores, and G_{ij} and $p_{t,ij}$ are the flow conductance and capillary entry pressure, respectively, for a throat connecting the i–j pore pair. Eq. (11) reflects the fact that liquid water transport occurs through a hydrophobic throat only when the capillary pressure is higher than the entry pressure of the throat.

The flow conductance, G_{ij}, in Eq. (11) was derived from the Hagen–Poiseuille equation as [36]:

$$G_{ij} = \frac{A_{w,ij}r_{t,ij}^2}{8\mu_w l_{t,ij}}, \tag{12}$$

where A_w is the flow area of liquid water in a rectangular throat, shown in Fig. 1(d), which is calculated as $A_w = A_t - A_a$. The flow area of air, A_a, was determined simply as:

$$A_a = r_{am}^2(4 - \pi). \tag{13}$$

A more complex expression for A_a, which considers the throat geometry and the contact angle, can be found in [36]. Nevertheless, Eq. (13) was sufficient for the present pore-network study.

The radius of the arc meniscus in the throats, r_{am}, can be determined from the capillary pressure in the upstream pore, p_c^{up}, as:

$$r_{am} = \frac{\sigma|\cos\theta_w|}{p_c^{up}}. \tag{14}$$

A simpler approach was used in this study, i.e., r_{am} was obtained by substituting p_c^{up} with the capillary entry pressure of the throat, p_t. From Eq. (9), a constant r_{am} is calculated for a throat as:

$$r_{am} = \frac{1}{2}r_t. \tag{15}$$

Although Eq. (15) neglects the variation of the flow area in throats according to capillary pressures, the changes in flow area are expected to be very small.

In the calculation of Eq. (10), an alternative expression for $Q_{i\to j}$ was used instead of Eq. (11):

$$Q_{i\to j} = G_{ij}(p_{c,i} - p_{c,j}) + G_{ij}[\max(0, p_{t,ij} - p_{c,i}) - \max(0, p_{t,ij} - p_{c,j})]. \tag{16}$$

The first term in the right hand side of Eq. (16) was included in the coefficient matrix of the algebraic governing equations, while the second term was included in the source vector. Using this approach, the diagonal dominance of the coefficient matrix required for iterative calculation was satisfied but a strong under-relaxation was needed due to the highly non-linear source term in Eq. (16).

A constant volume flow rate of liquid water, Q_{inj}, was imposed at the inlet boundary for calculation as:

$$Q_{inj} = \frac{M_w}{\rho_w} \frac{j_e}{2F}(1 + 2\alpha_{eff})A_{d,xy}, \tag{17}$$

where M_w is the molecular mass of water (0.0182 kg mol^{-1}); ρ_w is the density of water, j_e is the operation current density (A m^{-2}); F is the Faraday constant (96,487 C mol^{-1}); α_{eff} is the effective electro-osmosis coefficient; $A_{d,xy}$ is the planar area of the domain, $L_x \times L_y$. For simplicity of presentation, α_{eff} was set to 0. For the uniform flux boundary, the flow rate in Eq. (17) was equally divided by the number of invaded inlet pores, N_{inv}, then Q_{inj}/N_{inv} was assigned to each of the invaded pores. For the uniform pressure boundary, the entire Q_{inj} was assumed to be assigned to a virtual reservoir cell. A bisect method was used in the calculation to find the capillary pressure of the virtual reservoir cell that resulted exactly in the outflow of Q_{inj}.

Once a converged pressure field was obtained, the result was used to check if additional throats became invaded by liquid water. If so, the percolated clusters were updated to include those newly invaded throats and also pores connected to the throats. Thus, the capillary pressure calculation is the most computationally expensive step in the present pore-network model. On the other hand, the present pore-network model is, in fact, a simplified version in comparison with previous transient pore-network models [28–30] used for water transport in GDLs. A fully transient model requires a much higher computational cost due to very small time steps of about 10^{-6}–10^{-5} s to ensure the solution stability, in addition to a relatively long physical time of about 60 s to reach the steady-state [30].

Transient phenomena, such as capillary burst flow, cannot be captured using the current simplified pore-network model. It is considered, however, that the present pore-network model efficiently predicts the time-averaged steady saturation level in GDLs with reduced computational costs.

2.3.3. Saturation determination

At the end of the two-phase flow calculation, the pores and throats in a pore-network invaded by liquid water were identified along with the capillary pressures within those pores. The final step was to sum the liquid water volume in those pores and throats to obtain the saturation distribution in the pore-network. For this, the liquid water contents in the cubic cells depicted in Fig. 1(a) were determined first. The volume of liquid water in a cubic cell i, $W_{c,i}$, can be calculated as:

$$W_{c,i} = W_{p,i} + \sum_{j=\text{neighboring six pores}} \frac{1}{2}W_{t,ij}, \tag{18}$$

where $W_{p,i}$ is the liquid water volume in a pore i (the same index is used for a cubic cell and a box-shaped pore), and $W_{t,ij}$ is the liquid volume in throat-connecting pores i and j. A simple way of determining $W_{p,i}$ and $W_{t,ij}$ is to set $W_{p,i} = V_{p,i}$ or $W_{t,ij} = V_{t,ij}$ when a pore or a throat is invaded by liquid water.

In this study, a different approach was used to determine $W_{p,i}$ and $W_{t,ij}$ in order to be consistent with the pore-network geometries shown in Fig. 1. The liquid water volume in an invaded throat was calculated as:

$$W_{t,ij} = A_{w,ij} \times l_{t,ij}, \tag{19}$$

where $A_{w,ij}$ is the flow area of liquid water in throats determined during the preceding two-phase flow calculation. The liquid water volume in an invaded pore was determined as:

$$W_{p,i} = V_{p,i} \times S_w(p_c), \tag{20}$$

where $S_w(p_c)$ is the microscale relationship between the capillary pressure, p_c, and the saturation, S_w, in the box-shaped pores. An approximate equation for $p_c(S_w)$ used in Lee et al. [30] was employed to obtain $S_w(p_c)$:

$$p_c(S_w) = 2\sigma|\cos\theta_w|\left[\frac{3}{4\pi}\left(\frac{S_{tr}}{1-S_{tr}}\right)V_p(1-S_w)\right]^{-1/3} \quad \text{for} \quad S_w > S_{tr}. \tag{21}$$

The above equation was found to slightly overestimate S_w for a given p_c. Although a more accurate relationship could be used, Eq. (21) was believed to be sufficient for the present study. Note that a similar approach was also used by Thompson [39].

The determined $W_{c,i}$ in the cubic cells was then summed layer-by-layer and divided by the total void volume in the corresponding layer. This resulted in the layer-by-layer distribution of liquid water saturation. It should be noted that the current approach using Eqs. (19)–(21) does not guarantee more accurate saturation results than those obtained by the simpler method using $W_{p,i} = V_{p,i}$ and $W_{t,ij} = V_{t,ij}$. In fact, the determined saturation generally has less physical meaning in an absolute scale, but its relative level is important when investigating the effects of various conditions on water transport and saturation distribution.

3. Results

Geometrical parameters for the randomly generated isotropic pore-networks are summarized in Table 1. The size of the pore-networks was $20 \times 20 \times 10$, which corresponds to a GDL thickness, L_{GDL}, of 250 μm for $L_{cell} = 25$ μm. The distributions of pore volume, V_p, throat area, A_t, transition saturation, S_{tr}, and the throat length, l_t, in the simulated pore-networks are presented in Fig. 2. Number-mean values of several parameters are also provided in Table 1, along with their standard deviation (SD). The number-mean throat radius, $\bar{r}_t$, is about 5.33 μm in Table 1, which corresponds to an area-mean $\bar{r}_t$ of 5.95 μm. These values seem to be somewhat smaller than the measured volume-mean pore radius in GDLs, $\bar{r}_p$, of about 10 μm [41]. Thus, the capillary pressure is overestimated by about 70% in the present pore-network model compared with actual pressure in GDLs.

The present pore-network model determined the mean saturation distribution by averaging the results of independent simulations conducted for many different realizations. Thus, a total of 100 realizations were simulated for each uniform flux or uniform pressure condition to obtain both the mean saturation distribution and its standard deviation. Afterwards, only 10 realizations were simulated for each different situation to determine only the mean saturation distribution (10 realizations were sufficient to obtain a converged saturation distribution).

The mean porosity, ε, for the simulated pore-networks is estimated to be 0.633 (SD of 0.001) and the single-phase permeability, K, to be 3.39×10^{-12} (SD of 0.08×10^{-12}) m^2. Williams et al. [41] measured the through-plane permeability of carbon paper (TGP-H-120) with 75.6% porosity to be about 8.7×10^{-12} m^2. Similarly, Feser et al. [42] reported that the in-plane permeability of carbon
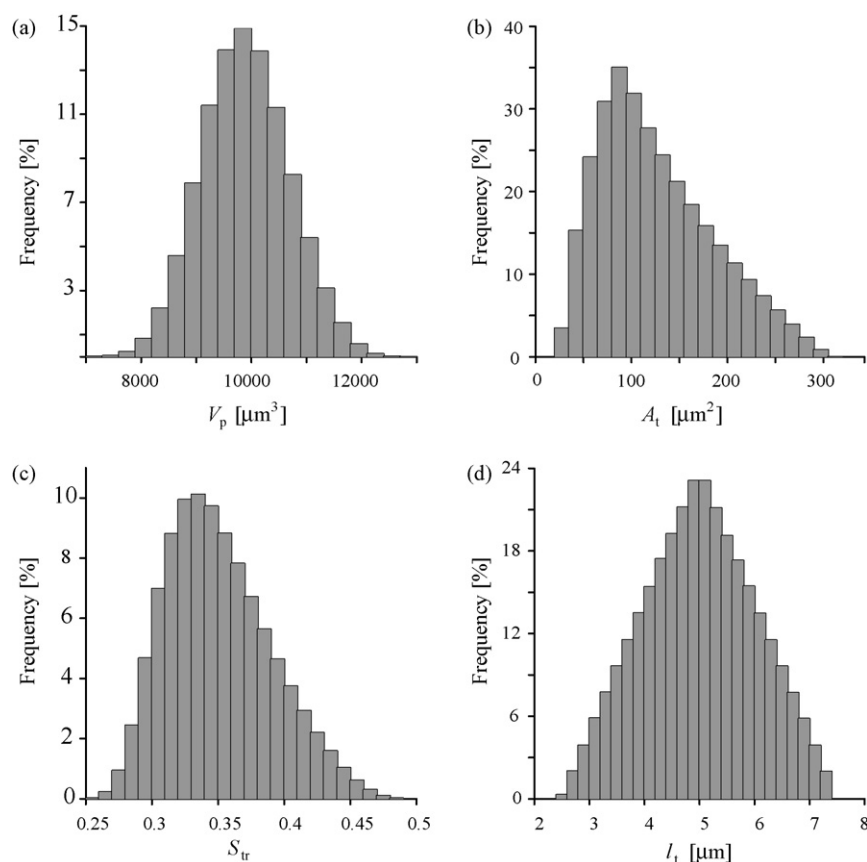
Fig. 2. Statistics of pore-network realizations: number frequencies of (a) pore volume, V_p; (b) throat area, A_t; (c) transition saturation, S_{tr}; and (d) throat length, l_t.

paper (TGP-H-60) amounted to about 5×10^{-12} m^2 for 70% porosity. Thus, the mean K of 3.39×10^{-12} m^2 seems to be reasonable, and indicates that the present pore-network model properly considers the pressure drop in GDLs due to viscous flow resistance.

3.1. Effect of inlet boundary condition

The two inlet conditions describing the liquid water entering hydrophobic GDLs were the uniform flux and the uniform pressure conditions. The uniform flux condition corresponds to a situation where the liquid water is introduced to a hydrophobic GDL as if it is directly injected into each inlet pore by means of many tiny needles. Thus, the liquid water flux is equally divided and uniformly distributed to all pores in the inlet boundary. The uniform pressure condition corresponds to a different situation where the liquid water is introduced to a hydrophobic GDL from a continuous reservoir in contact with the GDL. By increasing the pressure of the reservoir, liquid water is introduced to the hydrophobic GDL with a uniform source-side pressure distribution at the inlet boundary.

Fig. 3 shows the layer-by-layer distributions of liquid water saturation and capillary pressure obtained by averaging the results of 100 realizations for each uniform flux or uniform pressure condition. The symbols in Fig. 3 denote the mean values while the bared ranges denote the confidential limits of ± 2 SD (95.5%). The uniform flux condition results in a higher saturation level and also a higher capillary pressure than the uniform pressure condition.

In Fig. 3(a), the saturation distribution with the uniform flux condition shows an almost linear shape that connects the two points, wherein $S_w = 0.77$ close to the inlet boundary and $S_w = 0.06$ close to the outlet boundary. The average saturation for the entire domain was estimated to be 0.34. Note that this saturation distribution is similar to the steady-state saturation distribution obtained using

a transient pore-network model [30]. On the contrary, the saturation distribution with the uniform pressure condition shows a more concave shape in Fig. 3(a), where the saturation level is estimated to be 0.33 near the inlet boundary and 0.01 near the outlet boundary. Thus, the average saturation inside the entire domain is only 0.10 for the uniform pressure condition. Sinha and Wang [28] also predicted a similar saturation distribution based on a transient pore-network model.

The capillary pressure distribution also shows different shapes for the two boundary conditions in Fig. 3(b). The capillary pressure with a uniform pressure condition has an almost flat distribution at around 10 kPa, except near the outlet boundary. On the other hand, the capillary pressure distribution with a uniform flux condition shows a gradual decrease in pressure from 12.3 kPa near the inlet boundary to 10.5 kPa near the outlet boundary.

Detailed transport behaviour was investigated by inspecting the transport paths of liquid water in a pore network. For this purpose, an open-source Java viewer, Jmol, was utilized (http://www.jmol.org/). Fig. 4 illustrates the percolated clusters of invaded pores and throats, which are represented as balls and sticks, formed by liquid water injection with the uniform flux condition. Similarly, Fig. 5 shows the percolated clusters developed in a pore-network according to liquid water introduction under the uniform pressure condition. Note that two inlet conditions were applied to an identical pore-network for direct comparison. A comparison of the details given in Figs. 4(a) and 5(a) indicates that a more complicated flow pattern develops in the pore-network with a uniform flux condition than with a uniform pressure condition. Accordingly, the number of liquid water breakthroughs is also larger in Fig. 4(a) than that in Fig. 5(a).

When liquid water is uniformly injected into each inlet pore of a hydrophobic GDL according to the uniform flux condition, it ran-
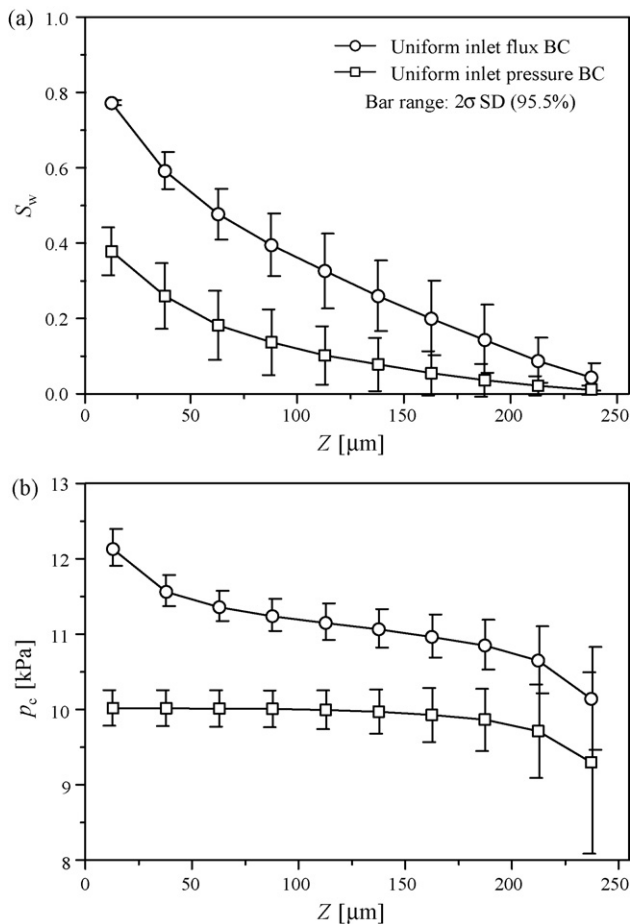
Fig. 3. Effect of inlet boundary condition on distribution of (a) liquid water saturation and (b) capillary pressure.

domly invades throats and pores in search of transport paths out of the GDL. Therefore, each of the invaded inlet pores has its own transport paths towards a liquid water breakthrough point. Thus, a steady-state is achieved only when all of the invaded inlet pores establish their own steady transport paths; this results in a longer transient time, a higher saturation level, and a higher area-specific number density of liquid water breakthroughs.

By contrast, the situation becomes very different when liquid water is introduced to a hydrophobic GDL from a liquid water reservoir, according to the uniform pressure condition. Inlet pores with larger dimensions are invaded first as the pressure of the reservoir is increased, followed by subsequent random invasion of liquid water through throats and pores. Once a single breakthrough path is established, however, the random invasion of liquid water stops and all of the liquid water flux is transported through that breakthrough path. Thus, a steady-state is achieved at the instant that the first breakthrough occurs; this results in a shorter transient time, a lower saturation level, and a smaller area-specific number density of liquid water breakthroughs.

In Fig. 4(a), the percolated clusters of invaded pores and throats have been given different colours according to the corresponding breakthrough points. Six breakthrough paths identified in Fig. 4(a) are individually plotted in Fig. 4(b) for better illustration. It can be observed in Fig. 4(b) that a breakthrough point is connected to several inlet pores in a certain region in the inlet boundary. If liquid water is injected into only one of those inlet pores, the corresponding breakthrough point is inevitably invaded. In other words, the injection of liquid water through six deliberately selected pores in the inlet boundary can open all six breakthrough points shown in
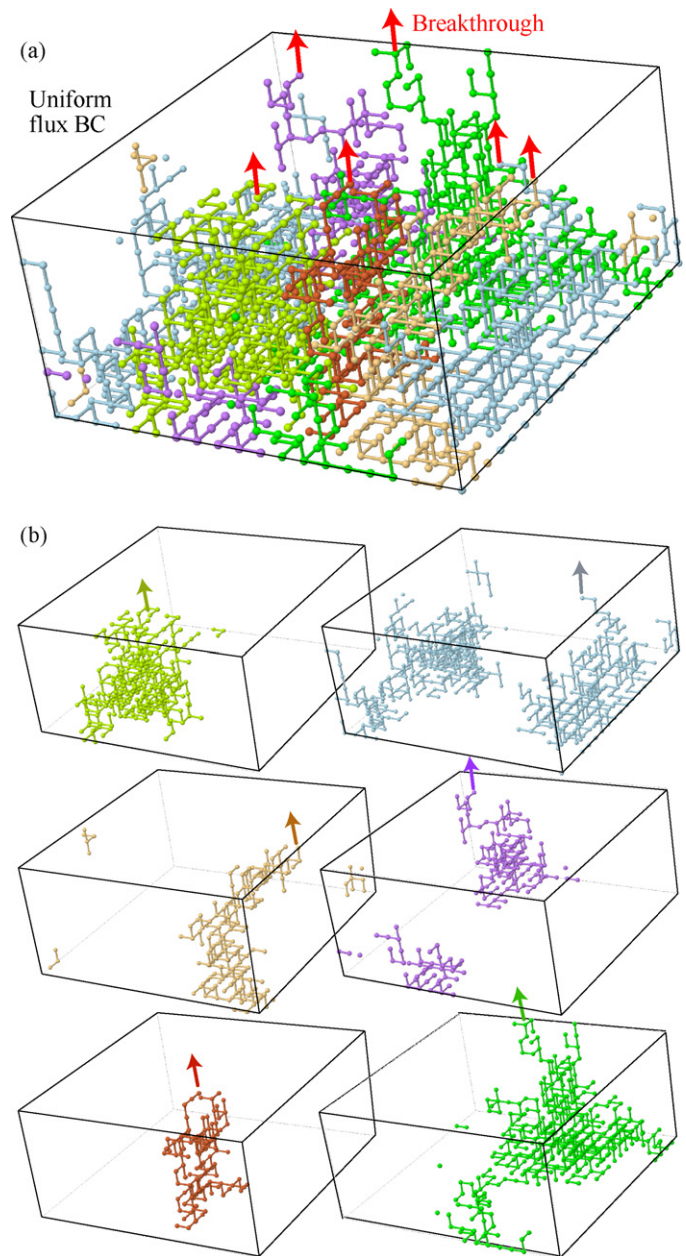

Fig. 4. Liquid water transport paths with uniform flux condition: (a) whole percolated clusters and (b) six individual clusters.

Fig. 4(a). Nevertheless, the flow pattern in that case is expected to be much simpler than that depicted in Fig. 4(a).

Most of the percolated clusters shown in Fig. 4(a) contribute to steady liquid water transport through the pore-network. By contrast, most of the percolated clusters illustrated in Fig. 5(a) are stagnant (dead-end clusters), and therefore do not contribute to steady transport. Fig. 5(b) presents only the active clusters that transport more than 1% of Q_{inj} introduced to the pore-network, which clearly indicates that only a few percolated clusters near the single breakthrough point participate in steady liquid water transport. It should also be noted that the liquid water flux entering the pore-network is highly non-uniform in a spatial sense, wherein only a small number of throats seem to be used for liquid water to enter the domain.

The approximate regions of liquid water residing in an identical pore-network are shown in Fig. 6. A Boolean flag variable, F_{inv}, was defined at the center of each unit cell and set to 1 when the pore
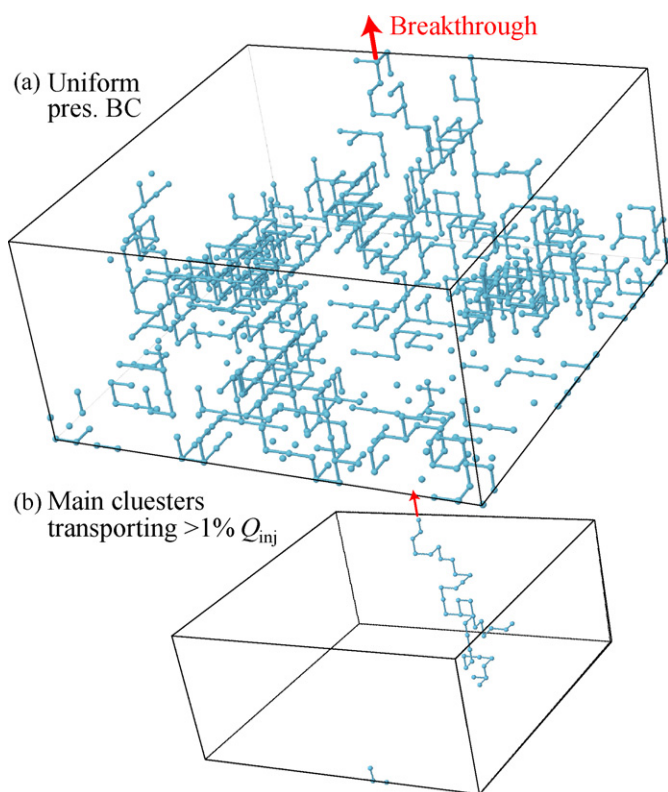
Fig. 5. Liquid water transport paths with uniform pressure condition: (a) whole percolated clusters and (b) active clusters transporting more than 1% of Q_{inj}.

in the unit cell was invaded (otherwise, F_{inv} was set to 0). The iso-surfaces corresponding to $F_{inv} = 0.5$ were then plotted. Although the presence of solid structures is ignored in Fig. 6, these iso-surfaces are believed to illustrate properly the approximate regions of liquid water distribution in a pore-network.

Fig. 6(a) corresponds to Fig. 4 for the uniform flux condition, and Fig. 6(b) to Fig. 5 for the uniform pressure condition. Note the identical locations of liquid water breakthrough points in Figs. 6(a) and 4, and those in Figs. 6(b) and 5. It is demonstrated again, in Fig. 6, that the uniform pressure condition results in a much smaller saturation distribution in the pore network compared with the uniform flux condition. As discussed above, most of the liquid water regions shown in Fig. 6(a) contributes to the steady transport, whereas most of the liquid water regions shown in Fig. 6(b) do not.

The validity of the two inlet conditions has been discussed previously by Lee et al. [30]. It was pointed out that a uniform liquid water pressure at the inlet boundary of a GDL is difficult to attain except when a continuous liquid water reservoir is in direct contact with the GDL. Nevertheless, the presence of a liquid water reservoir just beneath a GDL is not plausible since it will significantly hinder the diffusion of reactant gases towards a CL. In addition, the spatially non-uniform liquid water flux shown in Fig. 5(b) is incompatible with the rather uniform generation of liquid water in CLs. Therefore, the uniform flux condition is believed to provide a better description of the physical state of liquid water entering GDLs than the uniform pressure condition.

3.2. Effect of liquid water flux

The distributions of liquid water saturation and capillary pressure in pore-networks were obtained by varying the operation current density, j_e, as 2, 20, 200, 2000, and 20000 A cm^{-2}, as shown in Fig. 7. The operation current density is directly proportional to the liquid water flux through the GDL, as given in Eq. (17). For the
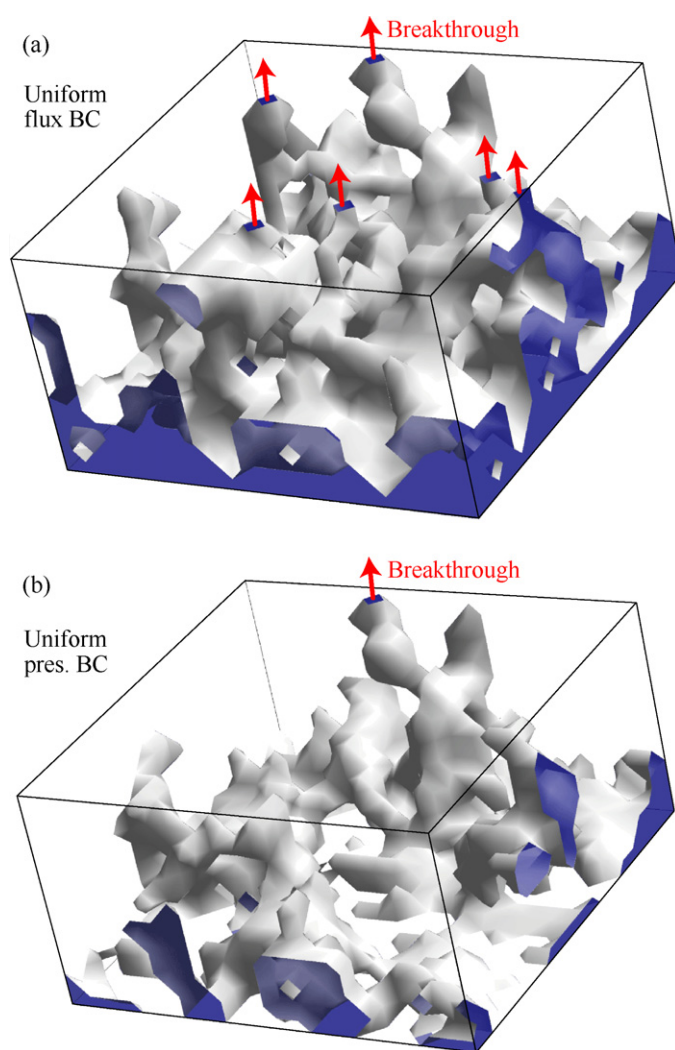

Fig. 6. Approximate regions of liquid water distribution with (a) a uniform flux condition and (b) uniform pressure condition.

uniform flux condition, Q_{inj} in Eq. (17) was divided as Q_{inj}/N_{inv}, and then Q_{inj}/N_{inv} was assigned to each invaded inlet pore that had been randomly selected. Note that Fig. 7 was obtained with $N_{inv} = N_x \times N_y$ ($P_{inv} = 100\%$).

The saturation distributions for j_e of 2 and 20 A cm^{-2} are almost identical in Fig. 7(a), and so are the capillary pressure distributions in Fig. 7(b). These results seem to be incorrect from the viewpoint of continuum two-phase flow models. Recall that the present pore-network model considers the capillary entry pressure and the viscous flow resistance as the primary parameters governing liquid water transport. The liquid water flux influences the viscous pressure drop but has no influence on the capillary entry pressure. Thus, the relative insensitivity of saturation distribution to liquid water flux can be interpreted as evidence that the transport is governed by capillary effects rather than viscous effects.

A current density of 2 to 20 A cm^{-2} corresponds to a capillary number, Ca, of about 2.5×10^{-8}–2.5×10^{-7}. As discussed earlier, such a small Ca with a viscosity ratio, M, of about 10 corresponds to the capillary fingering regime in the phase diagram for two-phase drainage flow [31]. Two-phase drainage flow in the capillary fingering regime is governed by capillary forces, resulting in a concave saturation distribution of an invading non-wetting phase. It was proposed that the concave saturation distribution originates from the invasion-percolation process [32].
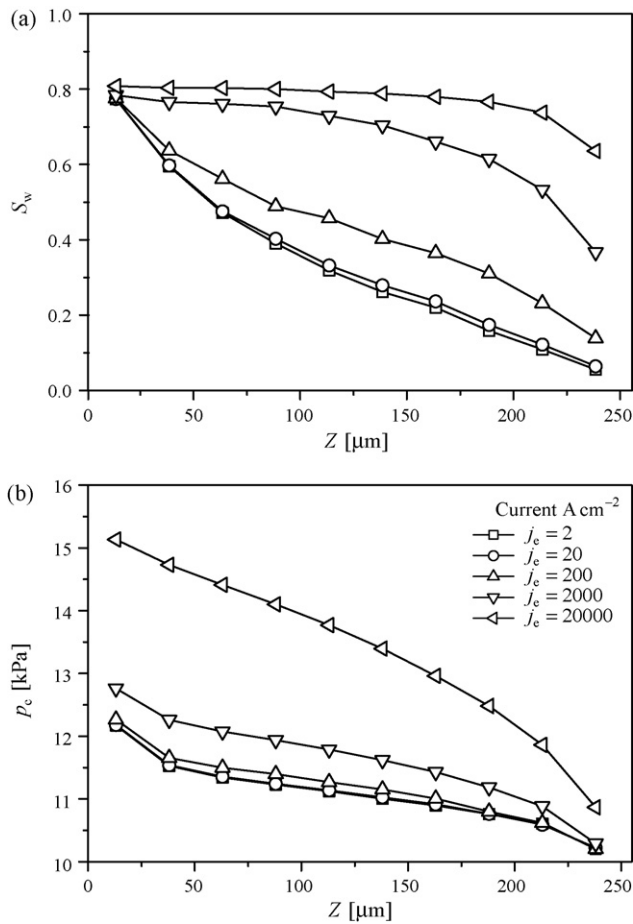
Fig. 7. Effect of liquid water flux, q_{inj}, on distribution of (a) liquid water saturation and (b) capillary pressure.

Fig. 8. Effect of invaded pore fraction, P_{inj}, on distribution of (a) liquid water saturation and (b) capillary pressure.

At a current density of $200\,\mathrm{A\,cm^{-2}}$, the saturation distribution still maintains a rather concave shape, but its level is slightly increased.

The saturation distribution changes into a convex shape when the current density, j_e, is increased to 2000 and $20000\,\mathrm{A\,cm^{-2}}$, as shown in Fig. 7(a). This transition in the saturation distribution from a concave shape to a convex shape indicates that the two-phase drainage flow gradually changes from the capillary fingering regime, where capillary forces are dominant, to the stable displacement regime, where viscous forces are dominant. The saturation distribution for j_e of $20000\,\mathrm{A\,cm^{-2}}$ has an almost flat shape around 0.8, which is a characteristic of the stable displacement regime. In addition, the capillary pressure distribution for j_e of $20000\,\mathrm{A\,cm^{-2}}$ is also rather linear, which indicates the dominance of viscous flow resistance. Thus, the transition in the flow regime seems to occur at a j_e of about $200\,\mathrm{A\,cm^{-2}}$, which corresponds to a Ca of about 2.5×10^{-6}. Sinha and Wang [28] also predicted a similar transition in the saturation distribution based on the uniform pressure condition.

3.3. Effect of invaded pore fraction at inlet boundary

Nam et al. [33] suggested that the liquid water saturation in a GDL depends on the number of liquid water breakthroughs at the inlet boundary of the GDL. Based on this argument, the water management role of MPLs was explained: MPLs reduce the area-specific number density of liquid water breakthroughs from CLs by merging many transport paths inside the MPLs. A similar explanation was also recently proposed by Gostick et al. [34]
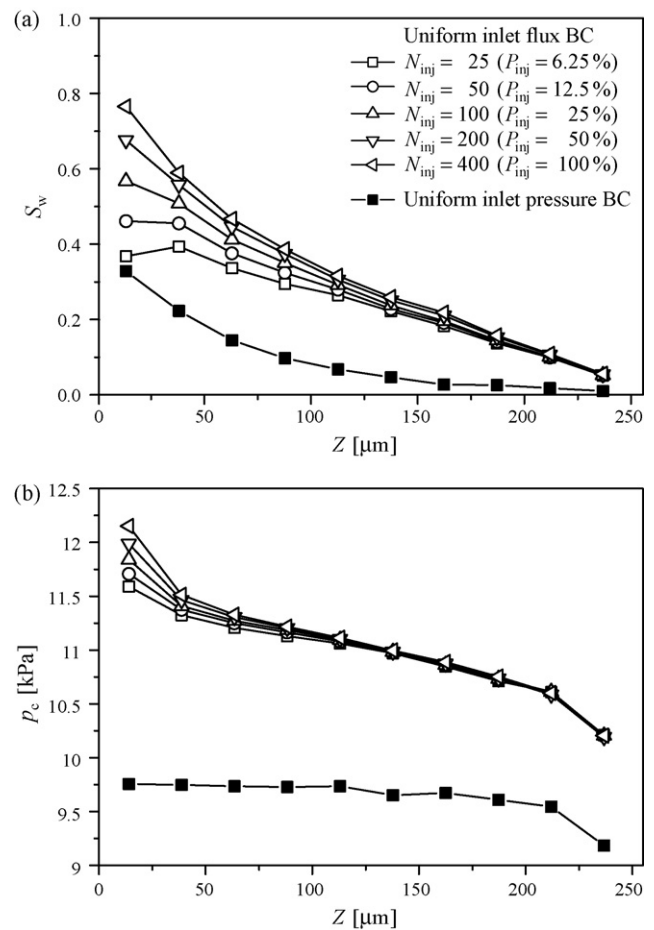
after experimentally examining liquid water transport in GDLs. In order to investigate this effect, the number of invaded inlet pores, N_{inj}, was varied as 400, 200, 100, 50, and 25 (for $N_{inj} < 400$, invaded pores were randomly selected among 400 inlet pores). The invaded pore fraction at the inlet boundary, P_{inj}, was also defined as:

$$P_{inj} = \frac{N_{inj}}{N_x \times N_y}. \tag{22}$$

Thus, the above N_{inj} correspond to a P_{inj} of 100, 50, 25, 12.5, and 6.25%. Note that $N_{inj} = 400$ ($P_{inj} = 100\%$) was used for the uniform flux condition in the previous sections.

Fig. 8(a) clearly indicates that a smaller value of P_{inj} results in a reduced saturation level in GDLs, especially near the inlet boundary. The saturation level near the inlet boundary was estimated to be 0.77 for $P_{inj} = 100\%$, 0.68 for $P_{inj} = 50\%$, 0.57 for $P_{inj} = 25\%$, 0.47 for $P_{inj} = 12.5\%$, and 0.37 for $P_{inj} = 6.25\%$. P_{inj} is observed to also influence the saturation level in far downstream regions, but the extent of this influence is not large. The capillary pressure distribution in Fig. 9(b) also shows a similar trend; capillary pressure near the inlet boundary is more sensitive to P_{inj} than near the outlet boundary. In Fig. 8(a), the uniform pressure condition generally results in a minimum saturation level during liquid water transport in hydrophobic GDLs.

Fig. 9 shows the percolated networks of invaded pores and throats in a pore-network for a P_{inj} of 100, 25, and 6.25%. As the invaded pore fraction increases, more complicated flow patterns appear to develop in the pore-network. This is because more paths are required for liquid water transport according to the increase in
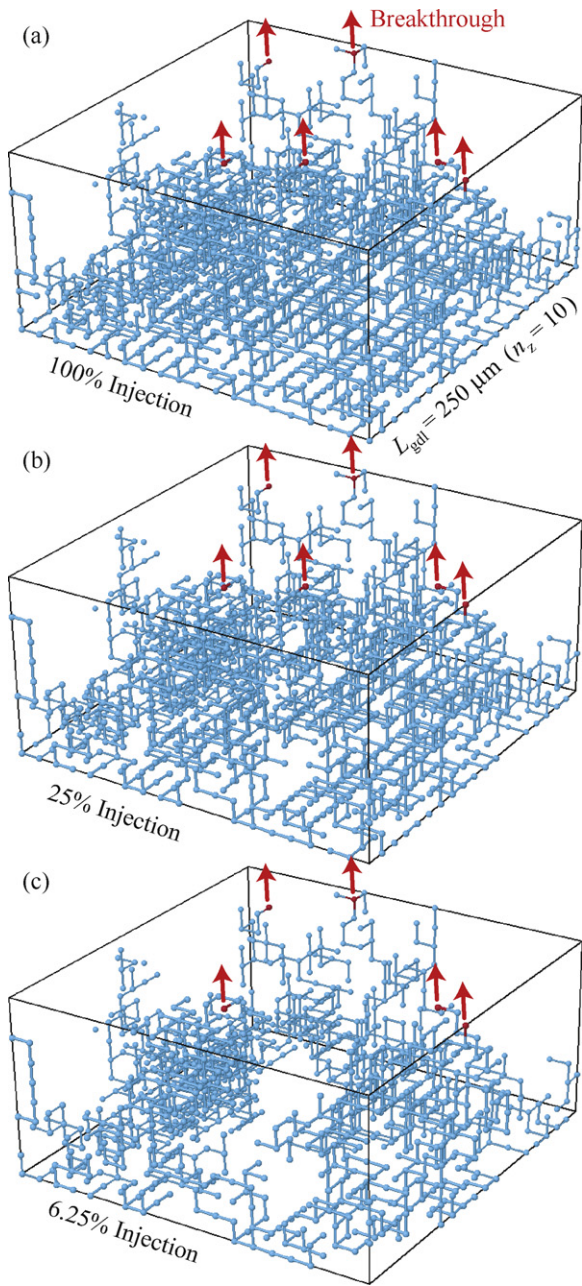
Fig. 9. Liquid water transport paths for invaded pore fraction, P_{inj}, of (a) 100%, (b) 25%, and (c) 6.25%.

Fig. 10. Effect of layer thickness, L_{gdl}, on distribution of liquid water saturation for invaded pore fraction, P_{inj}, of (a) 100%, (b) 25%, and (c) 6.25%.

the invaded pore number. The flow pattern near the outlet boundary is very similar, however, irrespective of the P_{inj} in Fig. 9. This is believed to be due to the merging of transport paths by the invasion-percolation process in the hydrophobic pore network. In fact, the number of liquid water breakthroughs is observed to be less sensitive to P_{inj}.

The results shown in Figs. 8 and 9 support the water management role of MPLs proposed by Nam et al. [33] and Gostick et al. [34]. In addition, the dependence of liquid water saturation in GDLs on P_{inj} also explains the increased saturation level in GDLs during the operation of PEMFCs at higher current densities.

3.4. Effect of GDL thickness

Fig. 10 shows the liquid water saturation obtained by varying the number of unit cells in the z-direction, N_z, as 6, 8, 10, 12, and
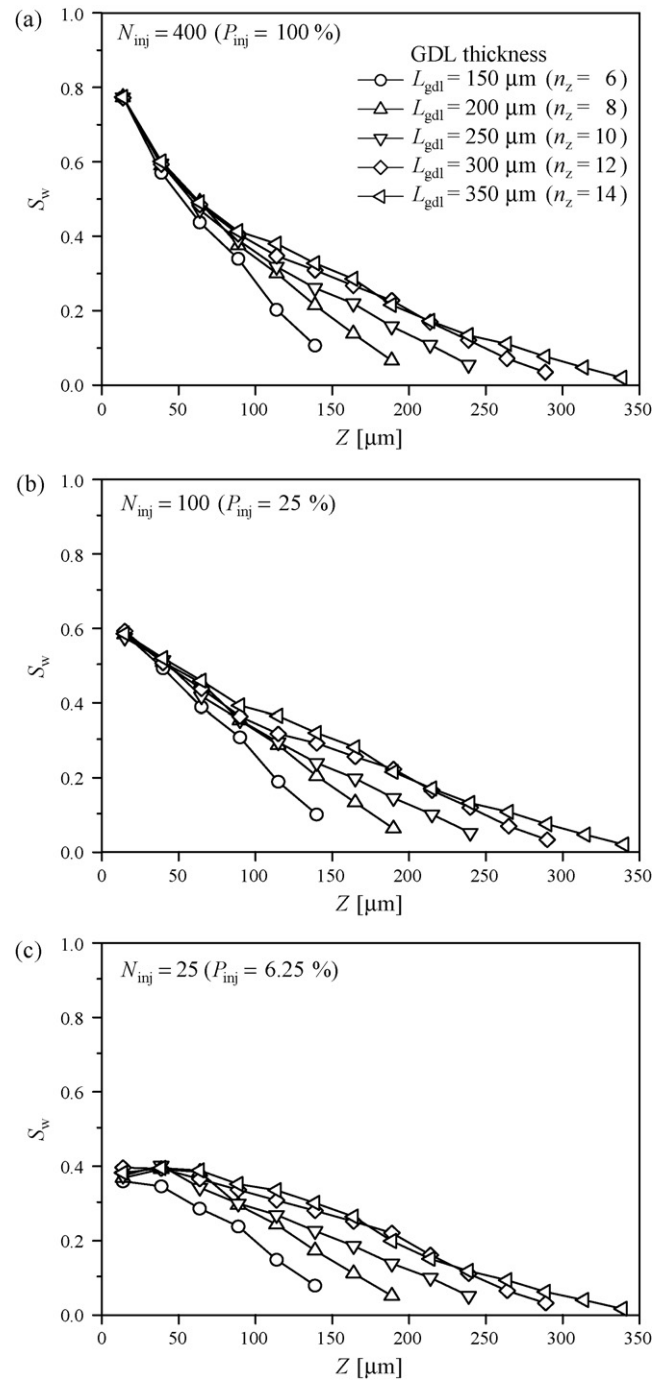
14. This pore-network modification corresponds to the situation where the thickness of a GDL, L_{GDL}, varies as 150, 200, 250, 300, and 350 μm. The data in Fig. 10 clearly indicate that liquid water saturation depends on the layer thickness, wherein a smaller thickness results in a lower saturation level in GDLs. The saturation level near the inlet boundary is less sensitive to the layer thickness compared with that near the outlet boundary. In addition, the saturation distributions for N_z of 12 and 14 are very similar. The effect of the invaded pore fraction, P_{inj}, in modifying the saturation distribution is also observed in Fig. 10.

The continuum two-phase flow theories generally correlate the increased layer thickness of porous media to the increased viscous
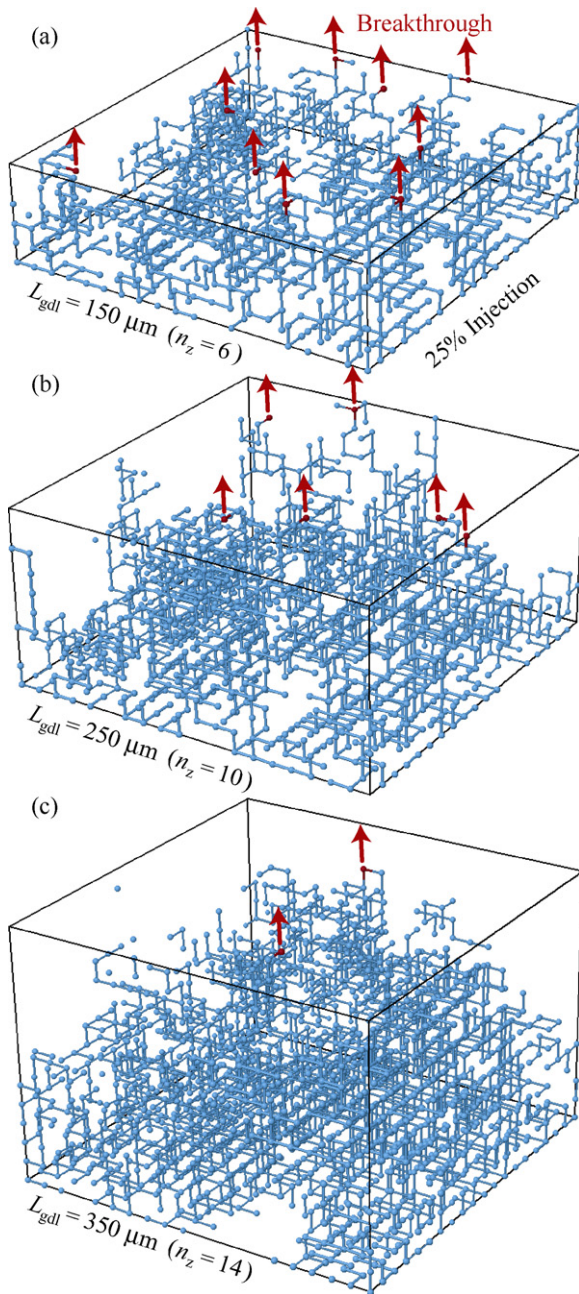
Fig. 11. Liquid water transport paths for layer thickness, L_{gdl}, of (a) 150 μm, (b) 250 μm, and (c) 350 μm.

flow resistance. Thus, a larger layer thickness requires a higher viscous pressure drop, thereby resulting in a higher saturation level. An alternative explanation can be made based on the invasion-percolation mechanism. The invasion-percolation of liquid water that searches for transport paths towards breakthrough points in the outlet boundary can be minimized when the porous media are thin. Accordingly, the flow structure becomes simpler as the thickness is reduced, resulting in a lower saturation level in GDLs.

The percolated networks of invaded pores and throats for N_z of 6, 10, and 14 are shown in Fig. 11, where the number of breakthrough points increases as the layer thickness decreases. This result indicates that the merging of transport paths appears to be hindered in thin porous media. A similar trend is also found in Fig. 10 that the saturation level near the outlet boundary increases as the layer thickness decreases. The saturation levels near the outlet are esti-

mated to be 0.02 for 350 μm, 0.04 for 300 μm, 0.06 for 250 μm, 0.07 for 200 μm, and 0.11 for 150 μm.

4. Discussion

The present results reconfirm the findings of previous pore-network studies [28,30] that liquid water transport in 'uniformly' hydrophobic GDLs is a strongly capillary-driven process. As discussed in [28,30], this conclusion is also consistent with the phase diagram for the two-phase drainage flow in porous media proposed by Lenormand et al. [31]. The invasion-percolation process [32] is thus believed to be the main transport mechanism for the capillary transport of liquid water in hydrophobic GDLs. In addition, the uniform flux condition is also found to provide a better description of the actual process occurring at the inlet boundary of GDLs compared with the uniform pressure condition.

Accepting the dominance of capillary processes, several aspects of liquid water transport in uniformly hydrophobic GDLs can be explained. A water generation rate equivalent to a current density of 2–20 A cm^{-2} is found to make almost no difference in the steady saturation distribution in Fig. 7. This result suggests that the liquid water flux in the range of normal PEMFC operation has less impact on the saturation level in GDLs. Instead, the data in Fig. 8 point out that the saturation level in GDLs depends on the number of invaded pores at the uniform-flux inlet boundary. The higher saturation levels in GDLs experimentally observed during the high current density operation of PEMFCs can then be explained by the increased number of liquid water breakthroughs from CLs.

The water management role of MPLs recently proposed by Nam et al. [33] and Gostick et al. [34] can also be explained by the dependence of the saturation level in GDLs on the invaded pore fraction. Many transport paths formed by the relatively uniform injection of liquid water from CLs are expected to merge inside the MPLs and thereby result in a significant reduction in the number of liquid water breakthroughs towards the GDLs. This process in MPLs is also inferred by Fig. 4, where the number of breakthrough outlet pores (six) is much smaller than that of invaded inlet pores (20×20). Thus, MPLs are believed to minimize the invaded pore fraction at the inlet boundary of GDLs, thereby leading to a reduced saturation level in the GDLs.

A smaller thickness is found to reduce the saturation level in GDLs, as shown in Fig. 10, which is understandable from the viewpoint of invasion-percolation transport. When the thickness of a GDL is small, it reduces the invasion-percolation process of liquid water that searches for transport paths toward breakthrough points. This trend is also observed by less complicated flow patterns obtained for smaller layer thicknesses, as shown in Fig. 11. The number of liquid water breakthroughs increases as the thickness of GDLs decreases in Fig. 11, which is consistent with the inverse proportionality between the area-specific breakthrough number density and the layer thickness suggested by Nam et al. [33].

Although not appropriate as an inlet condition, the uniform pressure condition is worth investigating because it leads to a minimum saturation level in GDLs. The condensation of water vapour inside GDLs is also important since it generally results in a higher saturation level than that required only for liquid water transport. Therefore, further studies are currently needed to resolve these issues from the viewpoint of invasion-percolation transport in GDLs. In addition, the effect of the mixed wettability in GDLs due to imperfect hydrophobic coating [29] also needs to be clarified in further studies.

5. Conclusions

Liquid water transport and saturation distribution in hydrophobic GDLs has been investigated by using a simplified pore-network

model combined with invasion-percolation path-finding and subsequent steady two-phase flow calculation. The pore-network results reconfirmed the dominance of the capillary process during liquid water transport in hydrophobic GDLs. The results also show that the saturation level in GDLs can be lowered by reducing the invaded pore fraction or by reducing the layer thickness. Several aspects of liquid water transport in uniformly hydrophobic GDLs are explained in terms of the invasion-percolation mechanism.

References

[1] J. Larminie, A. Dicks, Fuel Cell Systems Explained, John Wiley & Sons, New York, 2000.
[2] R.P. O'Hayre, S.W. Cha, W. Colella, F.B. Prinz, Fuel Cell Fundamentals, John Wiley & Sons, New York, 2006.
[3] A. Faghri, Z. Guo, Int. J. Heat Mass Transfer 48 (2005) 3891, doi:10.1016/j.ijheatmasstransfer.2005.04.014.
[4] H. Li, Y. Tang, Z. Wang, Z. Shi, S. Wu, D. Song, J. Zhang, K. Fatih, J. Zhang, H. Wang, Z. Liu, R. Abouatallah, A. Mazza, J. Power Sources 178 (2008) 103, doi:10.1016/j.jpowsour.2007.12.068.
[5] W. He, J.S. Yi, T.V. Nguyen, AIChE J. 46 (2000) 2053, doi:10.1002/aic.690461016.
[6] Z.H. Wang, C.Y. Wang, K.S. Chen, J. Power Sources 94 (2001) 40, doi:10.1016/S0378-7753(00)00662-5.
[7] L. You, H. Liu, Int. J. Heat Mass Transfer 45 (2002) 2277, doi:10.1016/S0017-9310(01)00322-2.
[8] T. Berning, N. Djilali, J. Electrochem. Soc. 150 (2003) A1589, doi:10.1149/1.1621412.
[9] J.H. Nam, M. Kaviany, Int. J. Heat Mass Transfer 46 (2003) 4595, doi:10.1016/S0017-9310(03)00305-3.
[10] U. Pasaogullari, C.Y. Wang, Electrochim. Acta 49 (2004) 4359, doi:10.1016/j.electacta.2004.04.027.
[11] A.Z. Weber, J. Newman, J. Electrochem. Soc. 152 (2005) A677, doi:10.1149/1.1861194.
[12] C. Ziegler, H.M. Yu, J.O. Schumacher, J. Electrochem. Soc. 152 (2005) A1555, doi:10.1149/1.1946408.
[13] J.T. Gostick, M.W. Fowler, M.A. Ioannidis, M.D. Pritzker, Y.M. Volfkovich, A. Sakars, J. Power Sources 156 (2006) 375, doi:10.1016/j.jpowsour.2005.05.086.
[14] A.Z. Weber, M.A. Hickner, Electrochim. Acta 53 (2008) 7668, doi:10.1016/j.electacta.2008.05.018.
[15] S. Litster, D. Sinton, N. Djilali, J. Power Sources 154 (2006) 95, doi:10.1016/j.jpowsour.2005.03.199.
[16] A. Bazylak, D. Sinton, Z.S. Liu, N. Djilali, J. Power Sources 163 (2007) 784, doi:10.1016/j.jpowsour.2006.09.045.
[17] S. Tsushima, K. Teranishi, S. Hirai, Electrochem. Solid-State Lett. 7 (2004) A269, doi:10.1149/1.1774971.
[18] P.K. Sinha, P. Halleck, C.Y. Wang, Electrochem. Solid-State Lett. 9 (2006) A344, doi:10.1149/1.2203307.
[19] R. Satija, D.L. Jacobson, M. Arif, S.A. Werner, J. Power Sources 129 (2004) 238, doi:10.1016/j.jpowsour.2003.11.068.
[20] N. Pekula, K. Heller, P.A. Chuang, A. Turhan, M.M. Mench, J.S. Brenizer, K. Ünlü, Nucl. Instrum. Meth. A 542 (2005) 134, doi:10.1016/j.nima.2005.01.090.
[21] C. Hartnig, I. Manke, R. Kuhn, N. Kardjilov, J. Banhart, W. Lehnert, Appl. Phys. Lett. 92 (2008) 134106, doi:10.1063/1.2907485.
[22] M.A. Hickner, N.P. Siegel, K.S. Chen, D.S. Hussey, D.L. Jacobson, M. Arif, J. Electrochem. Soc. 155 (2008) B427, doi:10.1149/1.2826287.
[23] C. Hartnig, I. Manke, R. Kuhn, S. Kleinau, J. Goebbels, J. Banhart, J. Power Sources 188 (2009) 468, doi:10.1016/j.jpowsour.2008.12.023.
[24] V.P. Schulz, J. Becker, A. Wiegmann, P.P. Mukherjee, C.Y. Wang, J. Electrochem. Soc. 154 (2007) B419, doi:10.1149/1.2472547.
[25] X.D. Niu, T. Munekata, S.A. Hyodo, K. Suga, J. Power Sources 172 (2007) 542, doi:10.1016/j.jpowsour.2007.05.081.
[26] J.T. Gostick, M.A. Ioannidis, M.W. Fowler, M.D. Pritzker, J. Power Sources 173 (2007) 277, doi:10.1016/j.jpowsour.2007.04.059.
[27] B. Markicevic, A. Bazylak, N. Djilali, J. Power Sources 171 (2007) 706, doi:10.1016/j.jpowsour.2007.06.053.
[28] P.K. Sinha, C.Y. Wang, Electrochim. Acta 52 (2007) 7936, doi:10.1016/j.electacta.2007.06.061.
[29] P.K. Sinha, C.Y. Wang, Chem. Eng. Sci. 63 (2008) 1081, doi:10.1016/j.ces.2007.11.007.
[30] K.J. Lee, J.H. Nam, C.J. Kim, Electrochim. Acta 54 (2009) 1166, doi:10.1016/j.electacta.2008.08.068.
[31] R. Lenormand, E. Touboul, C. Zarcone, J. Fluid Mech. 189 (1988) 165, doi:10.1017/S0022112088000953.
[32] M. Ferer, G.S. Bromhal, D.H. Smith, Physica A 319 (2003) 11, doi:10.1016/S0378-4371(02)01508-X.
[33] J.H. Nam, K.J. Lee, G.S. Hwang, C.J. Kim, M. Kaviany, Int. J. Heat Mass Transfer 52 (2009) 2779, doi:10.1016/j.ijheatmasstransfer.2009.01.002.
[34] J.T. Gostick, M.A. Ioannidis, M.W. Fowler, M.D. Pritzker, Electrochem. Commun. 11 (2009) 576, doi:10.1016/j.elecom.2008.12.053.
[35] M. Kaviany, Principles of Heat Transfer in Porous Media, 2nd ed., Springer, New York, 1999.
[36] S. Ma, G. Mason, N.R. Morrow, Colloids Surfaces A 117 (1996) 273, doi:10.1016/0927-7757(96)03702-8.
[37] D. Zhou, M. Blunt, F.M. Orr, J. Colloid Interf. Sci. 187 (1997) 11, doi:10.1006/jcis.1996.4699.
[38] C. Pan, M. Hilpert, C.T. Miller, Phys. Rev. E 64 (2001) 066702, doi:10.1103/PhysRevE.64.066702.
[39] K.E. Thompson, AIChE J. 48 (2002) 1369, doi:10.1002/aic.690480703.
[40] M. Singh, K.K. Mohanty, Chem. Eng. Sci. 58 (2003) 1, doi:10.1016/S0009-2509(02)00438-4.
[41] M.V. Williams, E. Begg, L. Bonville, H.R. Kunz, J.M. Fenton, J. Electrochem. Soc. 151 (2004) A1173, doi:10.1149/1.1764779.
[42] J.P. Feser, A.K. Prasad, S.G. Advani, J. Power Sources 162 (2006) 1226, doi:10.1016/j.jpowsour.2006.07.058.